Structure
Article

Crystal Structure of Type III Glutamine Synthetase: Surprising Reversal of the Inter-Ring Interface

Jason M. van Rooyen,[1,2,*] Valerie R. Abratt,[2] Hassan Belrhali,[3] and Trevor Sewell[1,4]
[1]Electron Microscope Unit
[2]Department of Molecular and Cell Biology
University of Cape Town, Rondebosch 7701, South Africa
[3]European Molecular Biology Laboratory, 38042 Grenoble Cedex 9, France
[4]Institute of Infectious Diseases and Molecular Medicine, University of Cape Town, Rondebosch 7701, South Africa
*Correspondence: jason@science.uct.ac.za
DOI 10.1016/j.str.2011.02.001

SUMMARY

Glutamine synthetases are ubiquitous, homo-oligomeric enzymes essential for nitrogen metabolism. Unlike types I and II, which are well described both structurally and functionally, the larger, type IIIs are poorly characterized despite their widespread occurrence. An understanding of the structural basis for this divergence and the implications for design of type-specific inhibitors has, therefore, been impossible. The first crystal structure of a GSIII enzyme, presented here, reveals a conservation of the GS catalytic fold but subtle differences in protein-ligand interactions suggest possible avenues for the design GSIII inhibitors. Despite these similarities, the divergence of the GSIII enzymes can be explained by differences in quaternary structure. Unexpectedly, the two hexameric rings of the GSIII dodecamer associate on the opposite surface relative to types I and II. The diversity of GS quaternary structures revealed here suggests a nonallosteric role for the evolution of the double-ringed architecture seen in all GS enzymes.

INTRODUCTION

The glutamine synthetases (GSs) are a family of large oligomeric enzymes catalyzing the condensation of ammonium and glutamate to form glutamine, the principal source of nitrogen for protein and nucleic acid synthesis. Because of their critical role in nitrogen metabolism, these enzymes are found in all forms of life from primitive to higher organisms (Pesole et al., 1991), and they may be among the most ancient functioning enzymes in existence (Kumada et al., 1993). Currently, GS enzymes are targets for the rational design of drugs against commercially and medically important organisms. A herbicide targeting GSII enzymes in plants (Glufosinate-ammonium from Bayer) has been commercially available for some time and research is currently under way to design selective inhibitors against the extracellular GSI secreted by *Mycobacterium tuberculosis* (Harth and Horwitz, 1999).

The GS family can be divided into three main enzyme types, easily distinguished by length: GSI with 360 amino acids on average, GSII with 450, and GSIII with 730. Interestingly, as more GS genes are discovered, it is becoming apparent that many organisms possess multiple enzymes from each type. For instance, enzymes with significant homology to GSI enzymes, which were previously thought to be limited to bacteria, have recently been identified in mammals and plants (Mathis et al., 2000; Wyatt et al., 2006). Equally, representatives of the GSII family, which were thought to be exclusive to eukaryotes, have also been found in free-living soil bacteria (Kumada et al., 1990). The most divergent type, namely, GSIII, with less than 10% global sequence identity to the type I and II enzymes, is the most recent to be recognized and is poorly characterized, despite their widespread occurrence. The GlnN protein from *Bacteroides fragilis,* an obligate anaerobe which is the primary causative agent of abdominal and systemic infections following trauma to, or surgery on, the digestive tract (Gibson et al., 1998) was the first GSIII isolated in 1986 (Southern et al., 1986). Homologous enzymes have subsequently been found in a wide range of evolutionarily diverse organisms including other anaerobic bacteria (Goodman and Woods, 1993; Xu et al., 2003; Amaya et al., 2005), photosynthetic blue-green alga (Reyes and Florencio, 1994), *Deinococcus radiodurans* (White et al., 1999), and the slime mold *Dictyostelium discoideum* (Eichinger et al., 2005). Of particular interest is the occurrence of GSIII enzymes in the medically and commercially important protozoans: *Trichomonas vaginalis* (Kinoshita et al., 2009), a highly prevalent human STI (Soper, 2004), and *Perkinsus marinus*, a pathogen of oysters (TIGR and the Center for Marine Biotechnology). As with the other GS types the type III enzymes do not always occur in isolation. For example, both GSI and GSIII are found in *Synechocystis* (Reyes et al., 1997).

Over the past five decades, extensive biochemical and (more recently) structural studies have built a picture of the mechanism and regulation of the GSI and GSII types (for a review, see Eisenberg et al., 2000). These studies have shown that all GS assemblies are composed of two closed ring structures (with active sites formed between protomers) which associate across an interface and are arranged with dihedral symmetry. GSI enzymes are all dodecameric oligomers with 622 symmetry, whereas the assignment of a consensus quaternary structure for the GSII enzymes has been controversial. Most recently, crystal structures from plants (Unno et al., 2006; Seabra et al., 2009), yeast (He et al., 2009), and mammals (Krajewski et al., 2008) have overturned

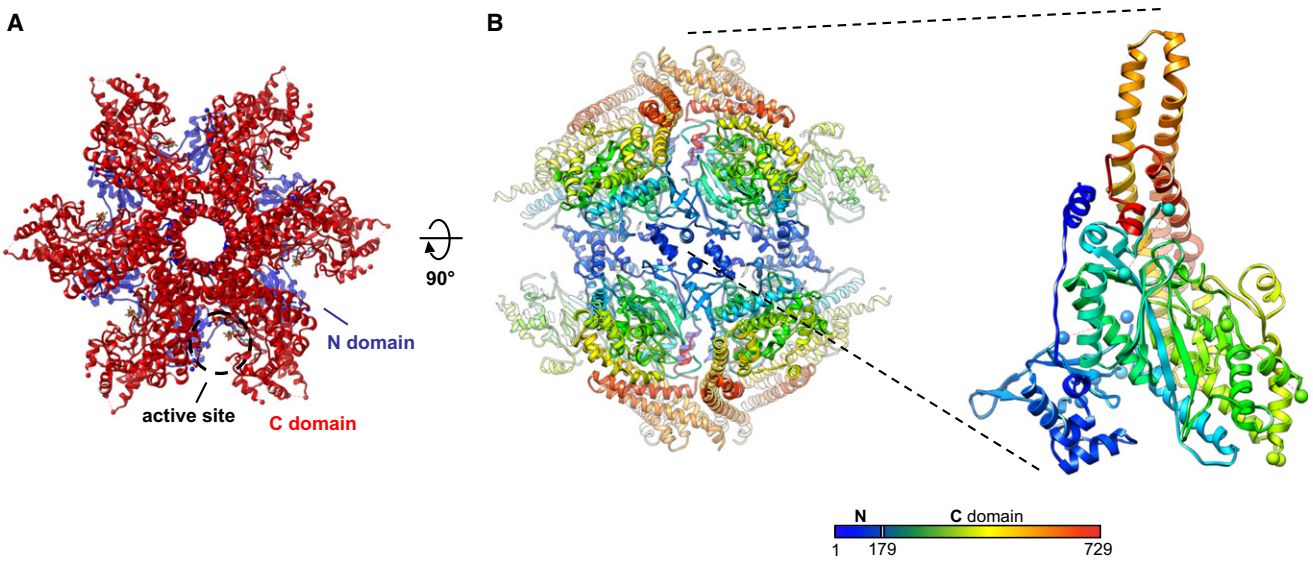

Figure 1. Crystal Structure of the *B. fragilis* GSIII Protein

(A) Axial view of the one of the two component hexamers of the GSIII protein shown in Cα ribbon representation with the N- and C-terminal domains colored blue and red, respectively. The ADP and MetSox-P ligands are visible in the active sites formed between these domains and spheres mark the end positions of missing density. (B) Equatorial view of the entire dodecamer colored according to residue position (as indicated in the key). A single monomer of the dodecamer is shown on the right and secondary structure assignments are given in Figure S2.

See also Figure S1.

the octameric assignments from early electron microscopy studies and revealed a decameric arrangement of subunits with 522 symmetry. To date, however, only low-resolution structural data exists to describe the type III GS enzymes, which are also double-ringed dodecamers (van Rooyen et al., 2006). This lack of atomic resolution structural data has prevented both an understanding of the basis for the sequence divergence of the GSIII enzymes and a structural evaluation of the possibility for the design of type III-specific inhibitors with potential application for the control of several important pathogens.

Following the development of a novel purification scheme for the untagged recombinant protein (van Rooyen et al., 2010) and the discovery of better diffracting crystals as a consequence of serendipitous proteolytic cleavage (van Rooyen et al., 2011), we have solved the crystal structure of recombinant GlnN protein from *B. fragilis* to 3.5 Å resolution. The first crystal structure of a GSIII enzyme reveals an unexpected quaternary structure change in the associating interface which not only explains the sequence divergence of the type III enzymes but also suggests that the conserved double-ringed architecture, seen throughout the family, does not play a role in GS regulation. The first structure-based sequence alignments for the GS family are also presented and show that despite the differences in quaternary structure, the GS catalytic fold and active site structure is conserved but subtle differences in ligand binding may be exploitable for type-specific inhibitor design.

RESULTS

Crystal Structure Solution

The GSIII structure (Figure 1; see Figure S1 available online) was solved using single wavelength anomalous dispersion and phase extension methods which utilized our previously reported dodecameric cryo-EM structure (van Rooyen et al., 2006) (Table 1; Figure S1). The final model comprises 87% of the *B. fragilis* protein, since several surface exposed loops are not visible in the electron density maps (discussed below), including the site of protease susceptibility (van Rooyen et al., 2011).

Catalytic Fold Conservation

The structure of the mostly α-helical monomer is similar in overall domain arrangement to previously determined GSI and GSII proteins. The whole protein has 12 β-barrel active sites each formed by the association of two β strands (**β3,4**) from the N-terminal (residues 1–178) and six β strands (**β6-8,10,12,13**) from the C-terminal domains (179–729) of adjacent subunits (Figure 1A). Throughout this work, conserved secondary structure elements (SSEs) are labeled numerically (Figure S2) and SSEs unique to each type of GS are labeled alphabetically in order of appearance in the structure, e.g., **GSI:βA**. Structural alignments of GSIII with the other GS structures (Figure 2) show that despite a low global sequence similarity to the other GS types (<9% global identity) several regions are highly conserved. Predictably, these are either components of the active sites or nearby loops. The latter, which are essential for catalysis and regulation (Eisenberg et al., 2000), are the most flexible in other GS structures and some also correspond to regions of missing density in the GSIII structure (Figure 3). Therefore, although the **β3-β4** loop (commonly referred to as the "latch" in GSI by Eisenberg et al., 2000), **β1-β2** loop, **α9-α11** "adenylylation loop," and **β6′-α4** "Y179 loop" are not seen in the GSIII structure, their absence is understandable in light of their flexibility and positions in the other structures and suggests a conservation of their topologies.

Table 1. X-Ray Data Processing and Structure Solution Statistics

Crystal Data	Ta_6Br_{12} Derivative[a]
Space group	$C222_1$
Cell dimensions	
a,b,c (Å)	199.20, 204.94, 235.03
α,β,γ (°)	90.00, 90.00, 90.00
Unit cell volume ($Å^3$)	10,329,709
Matthews coeff Vm ($Å^3$ Da^{-1})	2.62
No. mol a.s.u	6
Solvent content (%)	53.16
Data Collection	
Wavelength (Å)	0.933
Resolution range (Å)[b]	51.23–4.0 (4.22–4.00)
No. unique reflections[b]	40,502 (5855)[c]
No. observed reflections[b]	489,365 (68,876)[c]
Completeness (%)[b]	99.2[c]
Redundancy	12.1[c]
Signal/noise[b]	14.7 (6.3)[c]
R_{merge} (%)[b]	17.0 (39.2)[c]
R_{pim} (%) [a] (all I+ & I-)	5.3 (12.3)[c] [17.2][d]
Refinement	
Resolution range	62.87–3.50
Total no. reflections in refinement	60,072
No. reflections in test set	3,016
No. atoms	
Protein	30,720
Ligand/ion	276
Final R_{work}(%)	23.9
Final R_{free}(%)	26.9
Model Statistics	
Estimated coordinate error (cross-validated σA, 5.0–3.5 Å) (Å)	0.56
Rmsd	
Bond distances (Å)	0.009
Bond angles (degrees)	1.4
Dihendral angles (degrees)	20.7
Ramachandran torsion angle distributions (%)	
Favored regions	76.1
Allowed regions	20.2
Generously allowed regions	2.7
Disallowed regions	1.0
Average isotropic B-factor ($Å^2$)	37.7

$R_{merge} = \Sigma_{hkl} \Sigma i |I(h,i) - < I(h) > | / \Sigma_{hkl} \Sigma_i I(h,i)$.

$R_{pim} = \Sigma_{hkl} \sqrt{1/(N - 1)} \Sigma_i |I(h,i) - < I(h) > | / \Sigma_{hkl} \Sigma_i I(h,i)$ where N is the redundancy.

Signal/noise = < < I(h) > /sd < I(h) > > where < I(h) > is the (weighted) average over all observations for reflection h, and sd < I(h) > is the estimated SD of this average, after any "corrections."

[a] Native data were given previously (van Rooyen et al., 2011).

[b] Values in parentheses are for the highest resolution shell.

[c] Bijvoet pairs are unmerged.

[d] Value in square parentheses reflect Rpim (within I+/I-).

Protein-Ligand Interactions in the GSIII Enzymes

Electron densities, matching the positions of the ADP and L-methionine sulfoximine-PO_4 (MetSox-P) ligands in other solved GSI and GSII structures (Krajewski et al., 2005; Unno et al., 2006) together with two Mg^{2+} ions, are visible at the GSIII active site in maps calculated from unbiased density modified SAD phases (Figure 2, inset). However, high B-factors indicate that the occupancy of some parts of these ligands, such as the terminal phosphate of ADP, is quite low. In addition, four of the six essential residues involved in catalysis are not visible or unclear. Missing residues D129 and Y254 belong to the structural equivalents of the "latch" and the "Y179 loop" and there is only very weak density for the side chains of residues R460 (R339 is the equivalent residue in *S. typhimurium*) and R474 (R359 in *S. typhimurium*). There is also no density for the side chain of residue K281. In contrast, the important E327 and N264 residues, which belong to the "flap" and "N264" loop guarding the glutamate entrance to the active site, are clearly conserved in the corresponding *B. fragilis* GSIII residues E403 and N337, respectively. In total, 17 of the 33 residues found to interact with the metal ions, ADP cofactor, and MetSox-P inhibitor were conserved (Table S1).

The first structure-based multiple sequence alignments of the GS superfamily (Figure S3) show that the remaining 16 residues in the active site display a higher degree of sequence and conformational variability between GS structures. These differences reflect the varied modes of ligand recognition by the divergent GS types (Figure 4; Table S1). For the most part, these residues cluster around the ADP binding site in accord with analyses of GSI and GSII structures (Krajewski et al., 2008; Unno et al., 2006). This tolerance in side-chain orientation and chemistry can, in part, be explained since seven out of 18 of these residues interact with the ADP cofactor via their main chain atoms. Residues N334, R470, and F298 interact in a similar manner with the ligands in each GS type and so are not likely to confer selectivity. The remaining unique active site residues: A465, K281, A295, and N469, all interact with ADP via their side chains and, therefore, are likely to contribute the most to a type-specific mode of protein-ligand interaction (underlined residues in Figure 4A). In addition, GSIII, like GSII, has no structural counterpart to the backbone interaction between K361 and the purine ring of ADP, seen in GSI, because of the variability of the **β11-β12** region. Likewise, K215 in *M. tuberculosis* GSI interacts with the first phosphate of ADP but in *B. fragilis* GSIII, *Z. mays* GSII, and *S. typhimurium* GSI, the equivalent residue is threonine, glycine, or alanine (respectively) all of which are further than 4 Å away from the ligand. Therefore, although these two positions also appear to contribute toward varied protein-cofactor interactions between the enzyme types, they are similar in the GSII and GSIII structures.

Tertiary Structure Conservation

In addition to the obvious conservation of active site residues in the three GS structures, several regions of tertiary structure also share common architectures and topologies (colored SSEs in Figure 5). These more subtle structural conservations, which are not discernible from the sequence conservations alone, are evident when the structures are presented side-by-side. The GSIII proteins, therefore, share seven α helices and 13 β strands

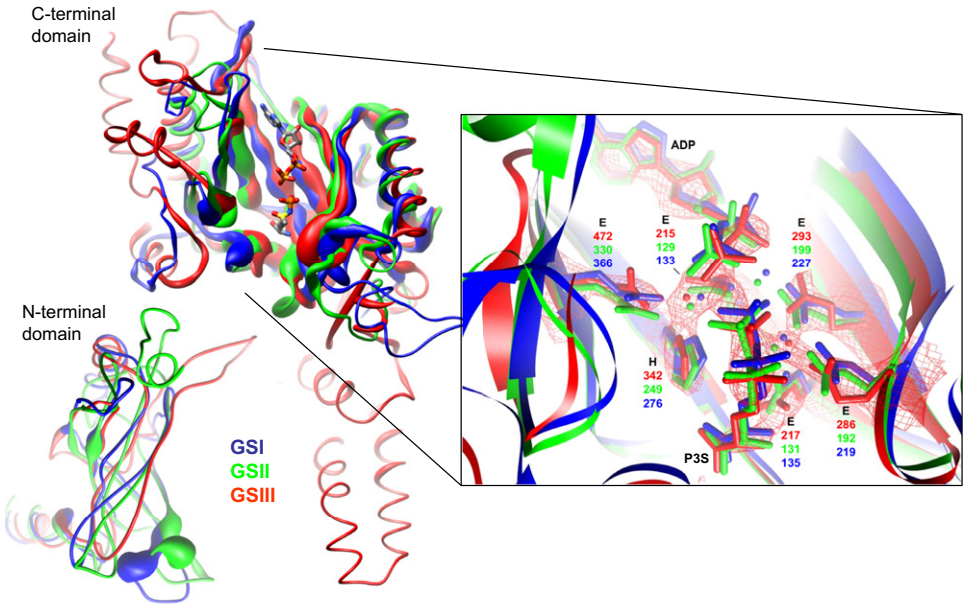

Figure 2. Conservation of Ligand Interactions

Superposition of the N- and C-terminal domains of *B. fragilis* GSIII (red), *S. typhimurium* GSI (blue) (Yamashita et al., 1989), and *Z. mays* GSII (green) (Unno et al., 2006) monomers. The width of the backbone represents the sequence conservation from the multiple sequence alignment in Figure S3 (8%–100%). The methionine sulfoximine phosphate (P3S) and adenosine diphosphate ligands are shown in stick representation. The orientation of the molecule is inverted relative to Figure 1B in accordance the commonly presented view of GS active sites. Inset, Highly conserved residues in the active sites of *M. tb* GSI (blue) (Krajewski et al., 2005), *Z. mays* GSII (green), and GSIII (red) structures are superimposed on the electron density of the latter (red wireframe).

with the other two GS types. This is in addition to the missing β strands (described above) which are predicted to be conserved on the basis of their sequence similarity. These conserved SSEs pack together to form the active-site β-barrel and, in so doing, create the conserved core region of the C-domain. The compact six-stranded N-terminal (β-grasp) domain is also well conserved and packs against the C-domain on the side opposite to the active site. Interestingly, an additional six α helices are shared only between GSI and GSIII structures with no structural counterparts in GSII.

Quaternary Structure Divergence

Surprisingly, despite sharing a conserved catalytic core with the other GS structures and consequently a conserved cyclic symmetry, the hexameric rings comprising the *B. fragilis* GSIII structure associate across opposite interfaces relative to the other GS types (Figure 6). As a result the active sites are positioned similarly within the rings but the inter-ring interfaces are contributed by opposite domains in GSIII (N-terminal) as compared to GSI (C-terminal); i.e., in GSIII, each ring has flipped 180° with respect to its position in the other two types. It is also apparent that, for the most part, the least conserved parts of the monomer structures are involved in higher order associations between subunits.

A detailed comparison of the residues responsible for higher order association in the three GS types is given in Figure 7. It is clear from this analysis that in no case do the same residues contribute to the inter-ring interfaces. In GSI, the inter-ring associations (red and orange contacts in Figure 7) mainly involve interactions of the eclipsed subunits on opposite sides of the ring interface (subunits **n** and **n′** interact over an interface area of 2648 Å^2). Isologous contacts from nonconserved SSEs, **GSI:βA-βB**, and the C-terminal helical "thong"(**GSI:αB**) are the main contributors to these interactions. Interactions with the diagonally positioned **n′+1** subunit, however, are less extensive (193 Å^2). In GSII, the **nth** subunit interacts weakly with the partially eclipsed **n′** (147 Å^2) and **n′+1** (185 Å^2) subunits and, as in GSI, a nonconserved mid-sequence loop region between **β6′** and **α4** is also responsible for isologous inter-ring contacts. In GSIII, however, the unique interfaces forming the inter-ring associations, which occur primarily between the **nth** subunit and the **n′-1** subunit in the opposite ring (880 Å^2) and to a lesser degree with the eclipsing **n′** subunit (168 Å^2), are all found in the N-terminal region. These unique insertions include a helix conserved in all GS types, **α1** (65–77), which interacts with symmetry equivalent helices, with a short loop between the nonconserved elements **GSIII:αB** and **αC** (39–50), and with the double-stranded **GSIII:βB-βC** (108–116) region. The latter interacts with symmetry related **GSIII:αB-αC** helices and the short **GSIII:α^{29}** helix, also interacts here in the **n′** subunit to stabilize this interface (Figure 8A).

The GSIII structure has also highlighted several significant differences in the interfaces between subunits within each ring, i.e., intra-ring interfaces (blue contacts in Figure 7). These are in addition to the subset of conserved intra-ring associations responsible for the common cyclic symmetry seen in all GS structures. In GSI, the **GSI:βA-βB** sheet region, mentioned above, associates with another nonconserved region, the short helix **GSI:αA** from the same nonconserved region in an adjacent subunit, to stabilize the hexameric rings (total intra-ring area of 1552 Å^2). In GSII, the N-terminal "meander" helix, **GSII:αA**, packs inside the central cavity within each ring to achieve

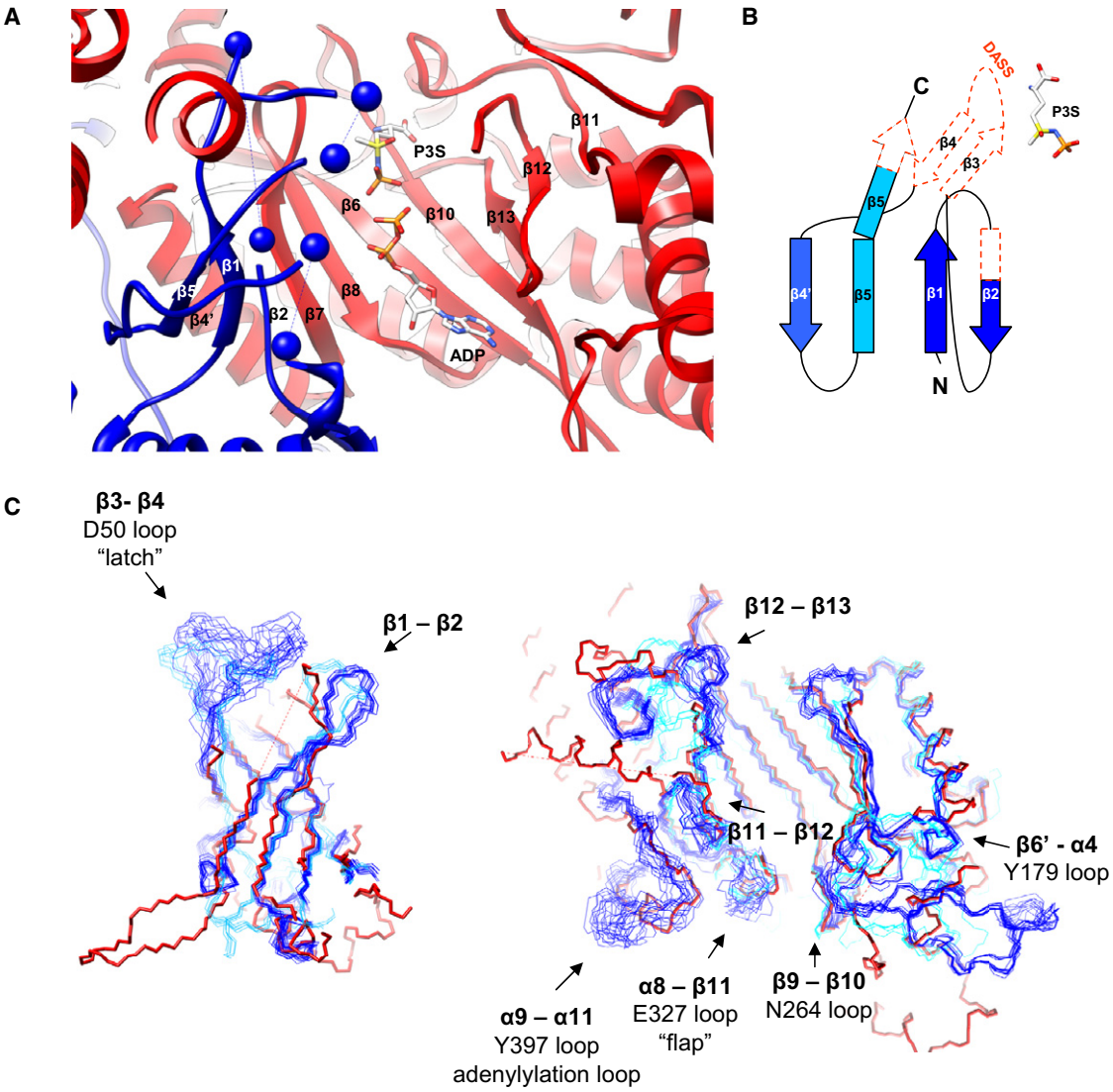

Figure 3. Structural Variability in the GS Crystal Structures

(A) Contributions of the N- (blue) and C-terminal (red) domains to the active site β-barrel. β strands are labeled as in Figure S2.

(B) β sheet connectivity diagram of the *B. fragilis* GSIII N-terminal domain. Only the main β strands forming the β-grasp motif are shown and the annotation of missing regions follows that of Figure S2 with the position of the MetSox-P (P3S) and ADP ligands indicated.

(C) Structural alignment of the N- (left) and C-terminal (right) domains of *B. fragilis* GSIII (thick red trace) against 17 GSI (thin dark blue trace) and six GSII (thin cyan trace) structures (see Experimental Procedures for details). The domains, Cα-backbone representation, are shown separately for the sake of clarity. The most flexible loops are labeled and important catalytic and regulatory loops discussed in the text are also indicated.

a similar increase in intra-ring contact area (1890 Å^2). GSIII, however, has the most extensive intra-ring subunit associations (2292 Å^2). The largest contribution is from the lengthy C-terminal extensions, which reach above the active site core regions to form dome shaped "caps" at either end of the complex (Figure 8B). Portions of the very long helices **α13** and **GSIII:αG** (617–667) interact with their symmetry equivalents from adjacent subunits to form this large contact area. Further down the cleft between subunits within each ring, **GSIII:loop^{716}** in the C terminus forms a metal ion binding site together with **α13** (612–615) as well as interacting with symmetry equivalents (Figure 8C). Finally, the C-terminal helix, **GSIII:αI**, also interacts with this metal ion binding loop and **α13** to further contribute to intra-ring stability. In addition to the contributions from the C-terminal region, several SSEs from the N-terminal and midsequence regions make intra-ring associations, including the N-terminal helix, **GSIII:αA** (1–17), the single turn helix segment, **GSIII:α^{29}** (22–32), the **GSIII:βB-βC** (108–116) double-stranded insertion, the helical segment **GSIII:α^{235}** (232–235), and the **GSIII:loop^{240}** (Figure 8D).

DISCUSSION

In this work, we set out to understand the structural basis of the sequence divergence of the large type III GS enzymes from the well-characterized type I and II enzymes and to ascertain

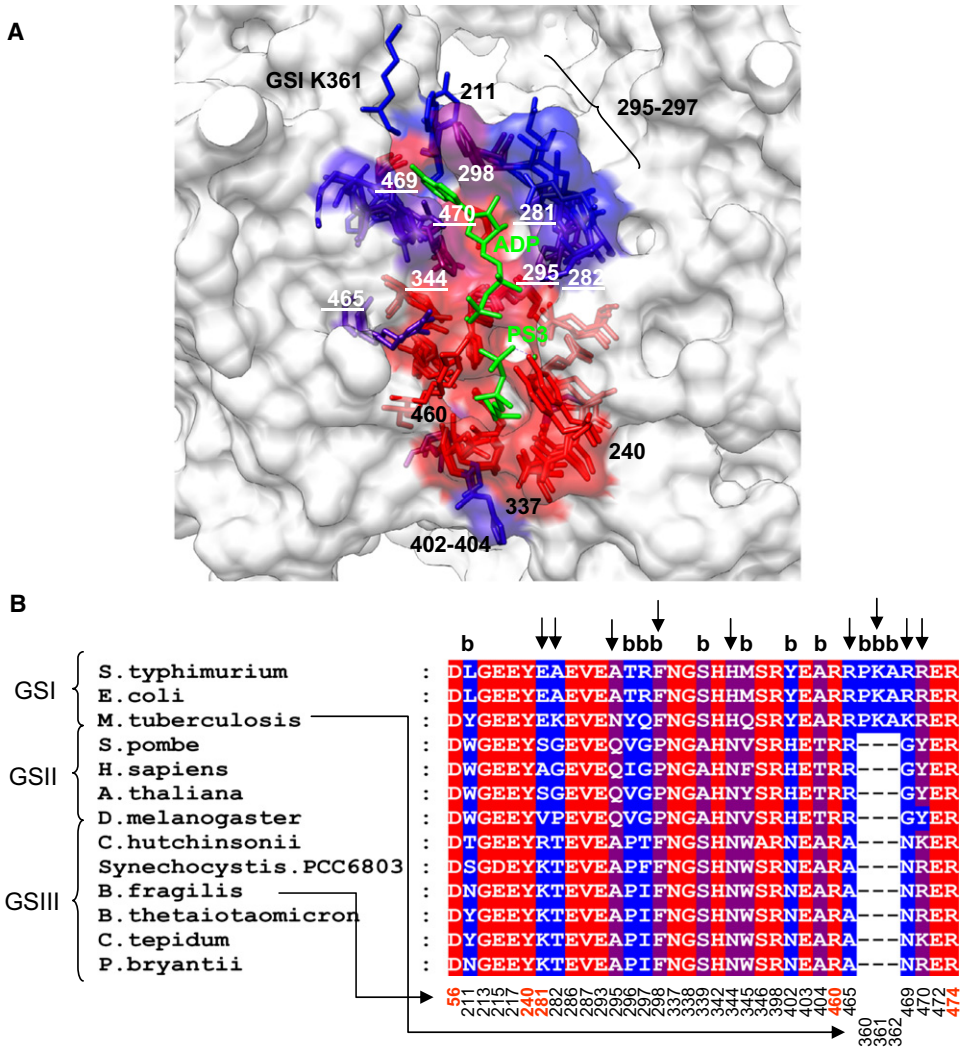

Figure 4. Conservation of Residues Responsible for Ligand Binding Specificity in the GS Family

(A) All of the residues that bind MetSox-P (P3S) and ADP and their homologous partners in the GS structures *B. fragilis* GSIII, *M. tb* GSI (Krajewski et al., 2008), and *Z. mays* GSII (Unno et al., 2006) are shown in stick representation and their degree of conservation is represented by their coloring (also projected onto the semitransparent surface). This coloring is mirrored in the MSA representing the percentage of conservation of the residues (linear scale between blue = 30% and red = 100%).

(B) MSA corresponding to (A). All active site residues are shown side-by-side and their numbering in the image follows that of the *B. fragilis* GSIII structure unless there is no counterpart, in which case, the numbering follows the *M. tb* GSI structure. Residues interacting with the ligands via main chain atoms are marked with a "b" above the MSA. Residues interacting with the ligands via side-chain associations are marked by arrows above the MSA and their respective labels are underlined in the image. Residues that were not visible or displayed weak side-chain density in the final electron density maps are highlighted in red below the MSA. The view is into the active site β-barrel from the direction of the N-domain matching the classic representations of GS active sites.

See also Table S1.

whether this divergence was sufficient to exploit in the design type-specific inhibitors. However, completely unexpectedly, the first crystal structure of a GSIII enzyme revealed a total nonconservation of the inter-ring interface of the dodecameric complex in comparison to the type I and II enzymes.

This discovery has important implications for the potential "druggability" of the type III enzymes. The fact that the majority of the sequence divergence of the GSIII enzymes can be attributed to changes in quaternary structure means that future efforts to design type-specific inhibitors will have to target the active site region because of the difficulties associated with disrupting protein-protein interactions. However, because the structure also showed that at the monomer level, the three GS types all share a highly conserved active site fold and 17 of the 33 active site residues, facts that confirm earlier bioinformatic analyses (Hill et al., 1989) and inhibition studies (Southern et al., 1987), the potential for successful selective inhibition relies heavily on the subtle differences in protein-ligand interactions identified within each family. Our detailed analyses of ligand-binding interactions suggest that several residues, K281, A295, N469, and

A654, represent the most promising avenues for the modification of existing compounds to achieve selectivity against the GSIII enzymes. Such type-specific inhibitors are needed to disentangle the additive contributions of multiple GS types and isoforms to nitrogen metabolism in the cellular context and to possibly control the industrially and medically important organisms which harbor GSIII enzymes.

The second major implication of the divergence of GSIII quaternary structure relates to our understanding of the evolution and role of quaternary structure in the functioning of these complex enzymes. All GS structures solved to date are large double-ringed structures with dihedral symmetry, as first summarized by Kretovich et al. (1984). The conservation of closed ring structures is understandable on the basis of the requirement that complete active sites can only be formed between protomers because of the opposing arrangement of the contributing N- and C-terminal domains. To date, however, the role played by the double-ring interface is uncertain. One suggestion has been offered by Eisenberg et al. (2000) who attributed the extensive inter-ring contacts in GSI to a role in homotropic cooperativity. Although, several lines of evidence exist to suggest that cooperativity is at play in the binding of metal ion cofactors and ligands in the GS enzymes (Denman and Wedler, 1984; Rhee et al., 1981; Shrake et al., 1980; Unno et al., 2006), we believe that the nonconservation of the inter-ring interface in GSIII indicates a noncatalytic or regulatory role for the convergent evolution of double-ringed GS structures.

Two principal findings have led us to this hypothesis. First is the almost identical positioning of active site β-barrels within each ring of the GSI and GSIII component hexamers (Figure 6A). Second is the conservation of **α1** and a portion of **α13** helices in GSI and GSIII, which play completely different roles in each structure. These regions are both major contributors to the inter-ring interfaces in GSIII and GSI, respectively, but are solvent exposed in their structural counterparts. In light of these findings, the simplest explanation for the existence of both the GSI and GSIII double-ringed dodecameric structures seen today is the evolution of isologous interactions on opposite sides of a catalytically functional single-ringed GS. Such an ancestor has already been suggested by Llorca et al. (2006) to have arisen via the fusion of two monomeric proteins, corresponding to the GS regulatory N- and catalytic C-terminal domains. If this hypothesis is accepted, then the double-ring interface must have evolved in response to driving forces other than specific catalytic or allosteric advantages effected through residue interactions between rings because it is the double-ringed structure itself and not the interface that is conserved.

Alternatively, several currently postulated theories for the emergence of higher order structures (for review, see Goodsell and Olson, 2000) seem to better explain the role of the double-ringed architecture in GS functioning. First, large proteins, which are most efficiently (for a given number of DNA base pairs) formed by oligomers, are thought to achieve higher stability through the cooperative action of multiple weak stabilizing interactions, thereby, avoiding the entropic costs of more rigid monomers (Monod, 1968; Lumry and Rajender, 1970). Notably, the nonconservation of the inter-ring interface in GSIII and the variety of intra-ring associations, found outside of the regions responsible for forming the conserved catalytic ring structures, suggest that these enzymes have converged toward large stable complexes. Studies have also shown that the different stabilities of various plant GSII isozymes can be attributed to mutations in a single residue (I161) involved in intra-ring contracts between adjacent subunits (Unno et al., 2006), thus providing clear evidence of the weak but cooperative nature of the oligomerization interfaces. The large number of flexible catalytic loops surrounding the almost identical active sites in all GS structures together with the extensive quaternary structure interfaces in the GS oligomers suggests that these enzymes have achieved stability without sacrificing the flexibility required for catalysis. A comparison of the interfaces in the three GS types (Table 2) shows that GSIII has the largest absolute contact surface area between protomers within its hexameric rings; the difference predominantly being contributed by the large domed caps at either ends of the dodecamer. Overall, however, the protomers in GSI are involved in the largest absolute interface surface areas followed by GSIII and then GSI. The second major consideration is that by burying a large percentage of their surface area upon oligomerization larger proteins are thought to limit deleterious interactions with other proteins such as nonspecific aggregations and susceptibility to proteolysis (Goodsell and Olson, 2000). In addition, it has also been suggested that the reduced surface areas of oligomers enhances the rate of catalysis by limiting the unproductive interactions of substrates with noncatalytic areas of the enzyme (Sharp et al., 1987). GSIII has the largest solvent accessible surface area (1.5 times larger than the next biggest: GSI) and as a consequence its protomers bury the least SA, 17% less than the GSI and GSII oligomers which both bury about 30% (Table 2). However, because of the small diameter of the openings at either end of the GSIII dodecamer's central cavity, only 60% of this SA is accessible to molecules with a radius larger than 3 Å. In contrast, 70% is accessible in the GSI and GSII structures for similarly sized probes. Therefore, the advantages resulting from reduced deleterious interactions with larger molecules like proteins and the smaller surface area presented to ligands still apply because of the GSIII enzyme's large central cavity.

Conclusions

This work has demonstrated that the divergence of the type III from the type I and II GS enzymes is mainly due to differences in quaternary structure despite all the enzymes sharing a remarkably conserved active site fold. Efforts to design type III-specific inhibitors will, therefore, have to focus on the subtle differences in protein-ligand interactions which we present here. The surprising inversion in the inter-ring interface of the GSIII enzymes suggests that the driving forces for the emergence of the double-ringed architecture seen in all GS enzymes cannot have been due to direct catalytic benefits achieved through long-range allosteric communication across the inter-ring interface. Instead, the resulting improved stability, more rigid active site geometries, and the minimization of exposed surface areas appear more likely to conferred selective advantages to these essential enzymes in the cellular context. The structural data and multiple sequence alignments presented here will provide the basis for future structural predictions of the many GSIII gene sequences currently in the databases and provide a framework for a large scale phylogenetic analysis of these ancient proteins.

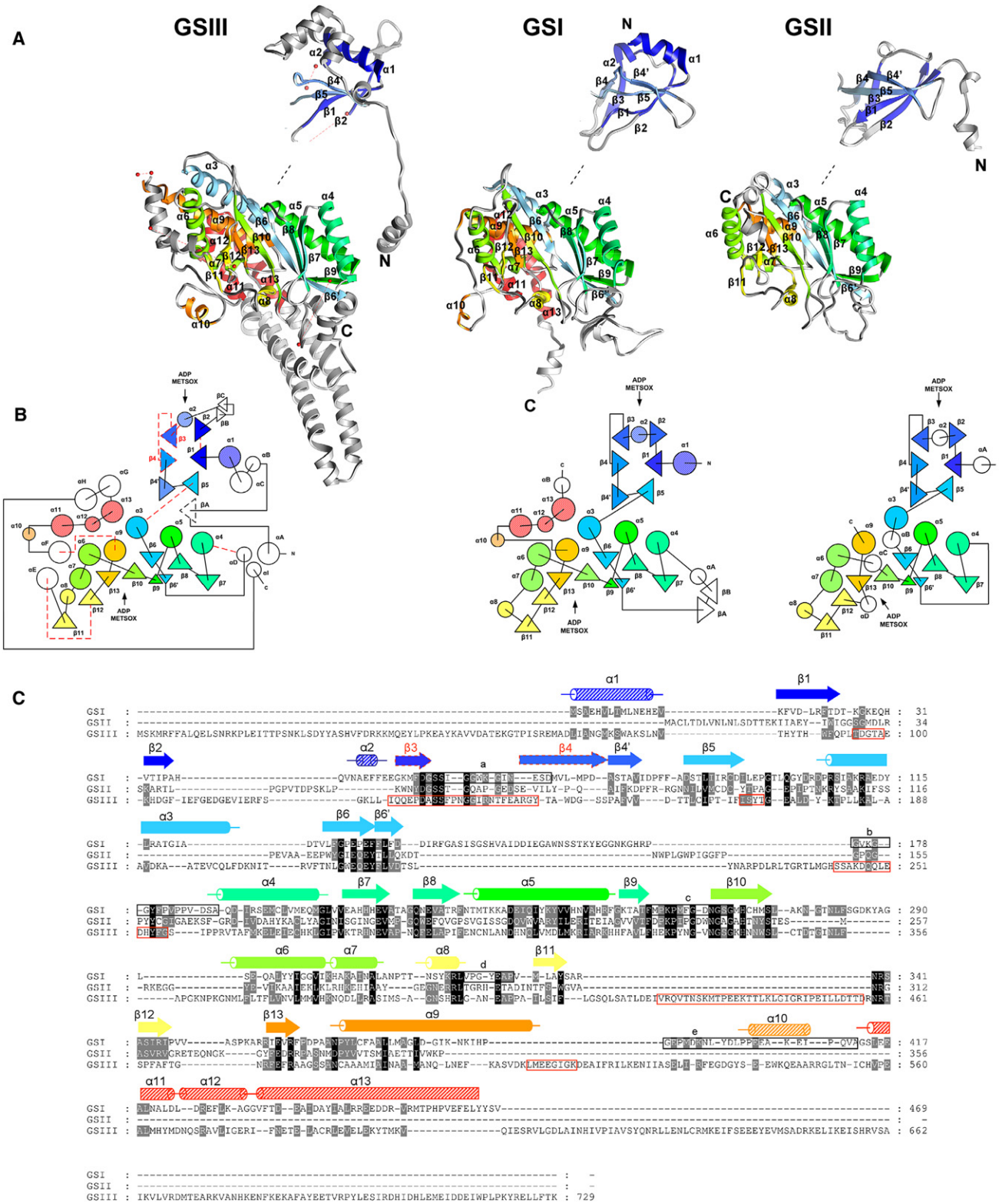

Figure 5. Architecture and Topology in the GS Structures

(A) Secondary structure elements common to all three GS types: GSIII, GSII (Unno et al., 2006), GSI (Yamashita et al., 1989), are numbered and colored according to sequence position (Figure S2). Nonconserved elements appear in grayscale and are labeled with letters in their respective structures. Missing residues are indicated by red dashed lines and the N-terminal domain has been separated from the C-terminal domain for the sake of clarity (black dashed line). The orientation of the GSIII monomer is inverted relative to Figure 1B because of the inversion in the inter-ring interface.

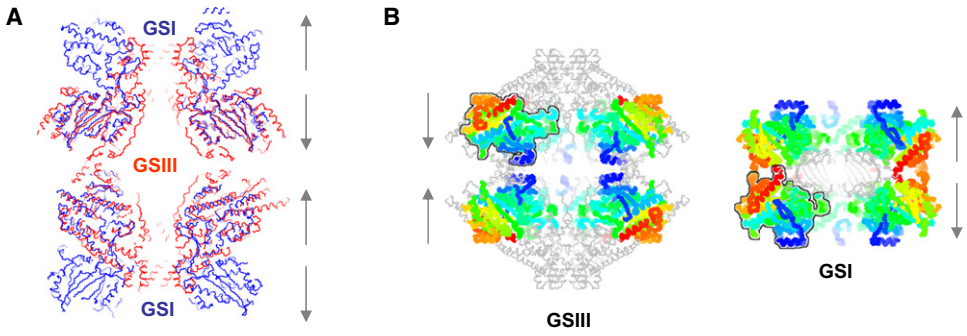

Figure 6. Inversion of the Inter-Ring Interface in *B. fragilis* GSIII

(A) Structural alignment, based on "A" chains only, of two *S. typhimurium* GSI (Yamashita et al., 1989) dodecamers (blue) and a single *B. fragilis* GSIII (red) dodecamer. Two GSI dodecamers are present in the alignment because of the inversion of the inter-ring interface in the two complexes. Gray arrows indicate the relative orientation of the component hexameric rings. Only a transverse central "slab" of the wireframe Cα structures is shown for clarity.

(B) Comparison of the conserved (colored as in Figure 5) and nonconserved (gray) SSEs of GSIII and GSI dodecamers. A transverse central "slab" of the wireframe Cα structures is shown for clarity. One pair of equivalent subunits from the alignment in (A) is outlined in black, and gray arrows indicate the relative orientation of the component hexameric rings.

EXPERIMENTAL PROCEDURES

Data Collection and Processing

Native data collection from a crystal of digested *B. fragilis* GSIII was performed as described previously (van Rooyen et al., 2011). Heavy atom derivitization was performed on the same crystals in situ for 30 min with 1 mM Ta_6Br_{12} (Jena Biosciences). Phasing data (4 Å) were collected at ID14-2 (ESRF) from a single crystal (0.1 mm) at 100 K with 0.933 Å wavelength X-rays. Integration of the data was carried out using iMOSFLM (Leslie, 2006), and space group assignments were evaluated in POINTLESS (Evans, 2005). Scaling, reduction, and merging of diffraction data were carried out using SCALA (Evans, 2005) within the CCP4 suite (CCP4, 1994).

Low-Resolution SAD Phasing and Phase Extension

Autosol within PHENIX (Adams et al., 2010) together with the programs HYSS (Grosse-Kunstleve and Adams, 2003), RESOLVE (Terwilliger, 2000), and PHASER (McCoy et al., 2007) were used to solve the initial structure of the single-wavelength anomalous dispersion (SAD) dataset from the derivitized crystal. Phase extension by iterative NCS averaging was then carried out with the scripts, AVEREST and SUPERMAP (A. Volbeda, unpublished work), kindly provided by Dr. Jorge Navaza and Dr. Stefano Trapani, which called on the Uppsala Software Factory package RAVE (Kleywegt et al., 2006) and the CCP4 suite of programs (CCP4, 1994) to carry out the multiple steps involved. A low-resolution "bead" model of the *B. fragilis* GSIII dodecamer was generated from an earlier cryo-EM reconstruction with the best matching handedness (van Rooyen et al., 2006) using SITUS (Wriggers et al., 1999) and then manually placed into the initial SAD-phased electron density map. The initial NCS parameters were obtained from the corresponding mask (calculated in MAMA) following an autocorrelation search using SUPERMAP using AMORE (Trapani and Navaza, 2008). The 7 Å SAD map was then averaged with AVE using these parameters and the mask updated with COMA and MAPMAN (all from USF RAVE; Kleywegt et al., 2006). Several hundred rounds of single crystal averaging with solvent flattening were then carried out using AVEREST. NCS operators were also improved during this process using IMP (Kleywegt et al., 2006). The resulting 7 Å phases from the averaged map were combined with the structure factors from the higher resolution native data set and phase extension was carried out from 7 to 3.5 Å (Figure S1).

Model Building

Initial model building was carried out automatically in Buccaneer (Cowtan, 2006) using the averaged 3.5 Å electron density. A maximum likelihood target function, incorporating phase information in the form of bimodal probability distributions, was utilized over the three cycles of model building. Manual editing, chain tracing, and fragment extension were then carried out in MIFit (McRee and Israel, 2008). Identification and connection of discontinuous density were aided by comparisons with GSI crystal structures (Yamashita et al., 1989; Krajewski et al., 2005) taking into account the multiple sequence alignments (MSA) produced by van Rooyen (van Rooyen et al., 2006) and secondary structure predictions from PSIPRED (McGuffin et al., 2000).

Crystallographic Refinement

Crystallographic refinement was carried out in CNS (Brunger, 2007) by NCS-constrained simulated annealing with torsion angle dynamics using data between 63 and 3.5 Å. Bulk solvent and overall anisotropic B-factor corrections were applied, and phase information, in the form of Hendrickson-Lattman coefficients (derived from the phase extended centroid phases and figures-of-merit by application of a B-factor 30 $Å^2$ and scale factor 0.75) were included with amplitudes in the maximum likelihood refinement target. Grouped temperature factor refinement (30 cycles) was then performed on the refined coordinates treating the main chain atoms and side-chain atoms as separate groups. The cross-validation subset (5%), assigned in CCP4 (CCP4, 1994), was excluded from the refinement.

The NCS operators were reoptimized by rigid body refinement of a hexameric model, generated using XPAND (USF X-UTIL) (Kleywegt et al., 2006). Phase extension (200 cycles of density truncation, solvent flipping, and NCS averaging 7–3.5 Å) was also repeated in CNS to produce phase probability distributions in the form of Hendrickson-Lattman coefficients rather than the bimodal distributions used initially.

Empty densities including the ligands ADP and MetSox-P, together with two Mg^{2+} ions and two Cl^- ions, visible in the averaged 3.5 Å map, were modeled on their counterparts in *Z. mays* GSII (Unno et al., 2006) and *M. tuberculosis* GSI

(B) Topology diagrams for the three GS structures. α helices are represented by circles, β strands by triangles, and striped annotations represent elements only conserved in the GSI and GSIII enzyme types.

(C) Structure derived multiple sequence alignment of the three GS structures. Conserved secondary structure elements (solid arrows: β strands or cylinders: α helices) are labeled as above and sequence conservation is represented by the grayscale shading. Missing residues in the *B. fragilis* GSIII sequence are outlined in red and missing secondary structure elements are outlined in red dashed lines and labeled in red text. Residues contributing to the five important loops, labeled a–e, mentioned in the text, are highlighted by black boxes.

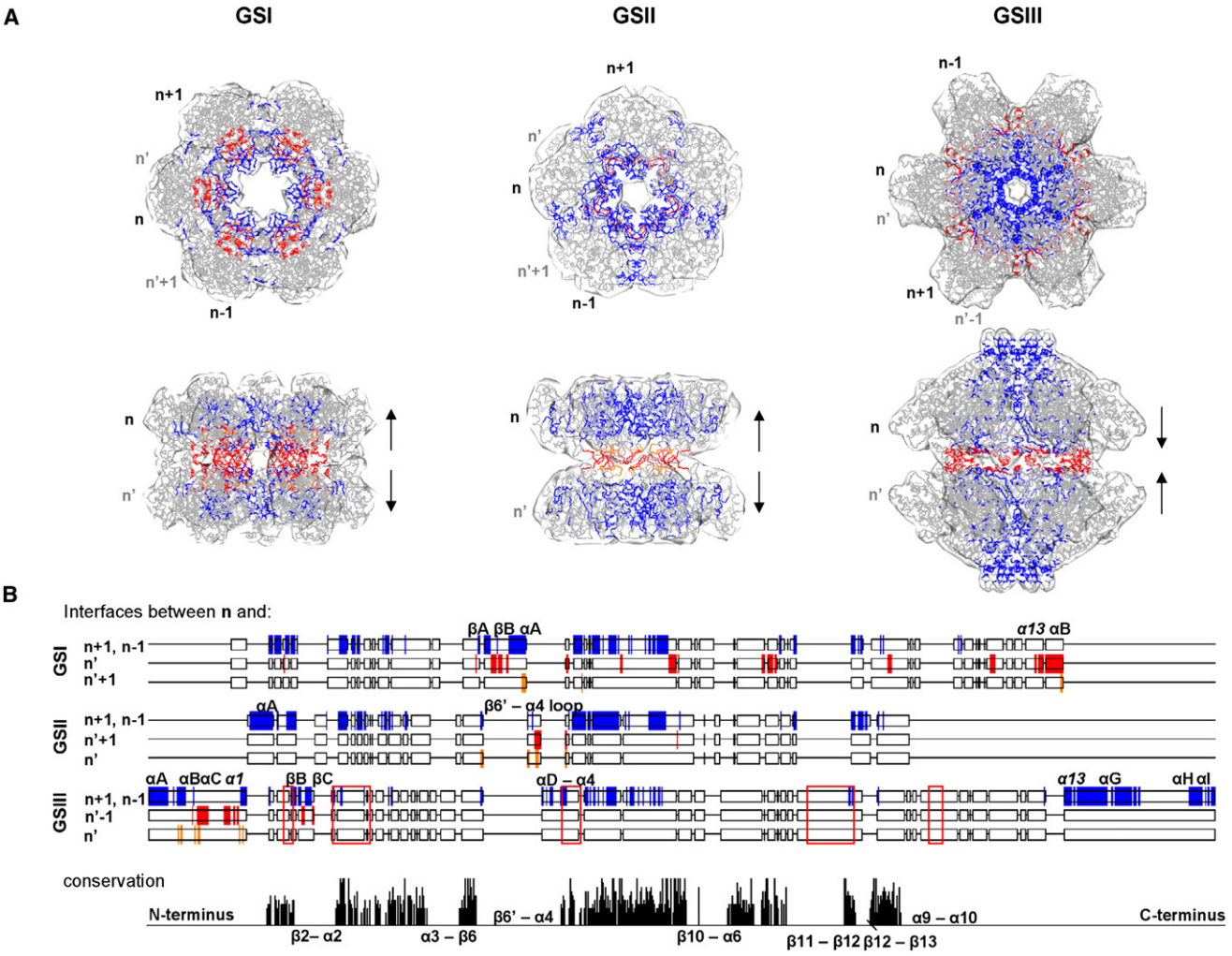

Figure 7. GS Quaternary Structure Interfaces

(A) Residues contributing to interactions between subunits are shown for GSIII, *S. typhimurium* GSI (Yamashita et al., 1989), and *Z. mays* GSII (Unno et al., 2006). Intra-ring contacts (blue) are between the $\mathbf{n}^{th}$ subunit and the subunits on either side within the ring, **n+1** and **n-1** (the numbering is positive in the direction of the N-terminal domain). Inter-ring contacts (red) are between the $\mathbf{n}^{th}$ subunit and the closest subunit in the opposite ring (marked with an apostrophe). In GSIII and GSI the diametrically opposite subunit to **n** is **n′**. In GSII, the **n′** subunit is the closest subunit in the opposite ring. Less substantial contacts between the $\mathbf{n}^{th}$ subunit and the subunits in the opposite ring (on either side of the **n′**) are colored orange. Black arrows indicate the relative orientations of the component rings of the oligomers.

(B) Locations of the residues involved in higher order associations indicated on the schematic multiple sequence alignments of the three GS structures (from Figure S2). The percentage conservation (0–11) is graphed below. Red boxes indicate the positions of missing density in the GSIII structure.

(Krajewski et al., 2005) structures in Coot (Emsley and Cowtan, 2004) and the occupancy of residue side chains without visible electron density was set to zero. The parameterization and topology files for refinement of these ligands were generated by PRODRG (Schuettelkopf and van Aalten, 2004). A process of manual model building and real-space refinement in COOT followed by refinement in CNS was then iterated until no further visual improvement in the match between the model and the electron density was achieved. The crystallographic refinement cycles were carried out on the entire hexamer with strong NCS restraints (weight 300 and sigb 2). All renderings of molecular coordinates and electron density maps were carried out in UCSF CHIMERA (Pettersen et al., 2004).

Structural Alignments

Multiple sequence alignments (MSAs) were derived from superposition of the *B. fragilis* GSIII monomer structure with *S. typhimurium* GSI (Yamashita et al., 1989) and *Z. mays* GSII (Unno et al., 2006) structures. N- and C-terminal domains from each structure were aligned separately using the MATCHMAKER feature in UCSF CHIMERA (Pettersen et al., 2004; Meng et al., 2006). The fit between this initial structure-based profile and the three aligned structures was then optimized by manual inspection and realignment of secondary structure elements in 3D space before presentation in the GENEDOC package (Nicholas et al., 1997). This initial structural alignment was used to construct a profile based multiple sequence alignment of representative members of the three GS families (Figure S3) and the percentage of conservation was plotted in Figure 4 using Jalview (Waterhouse et al., 2009). The origin of these sequences has been described previously (van Rooyen et al., 2006).

The alignment of GSIII to all of the current publicly available GS crystal structures was achieved in MULTIPROT (Shatsky et al., 2004) as described above. GSI structures included: 1f1h, 1f52, 1fpy (Gill and Eisenberg, 2001); 1lgr (Liaw et al., 1994); 2gls (Yamashita et al., 1989), 2lgs (Liaw et al., 1993); 1hto, 1htq

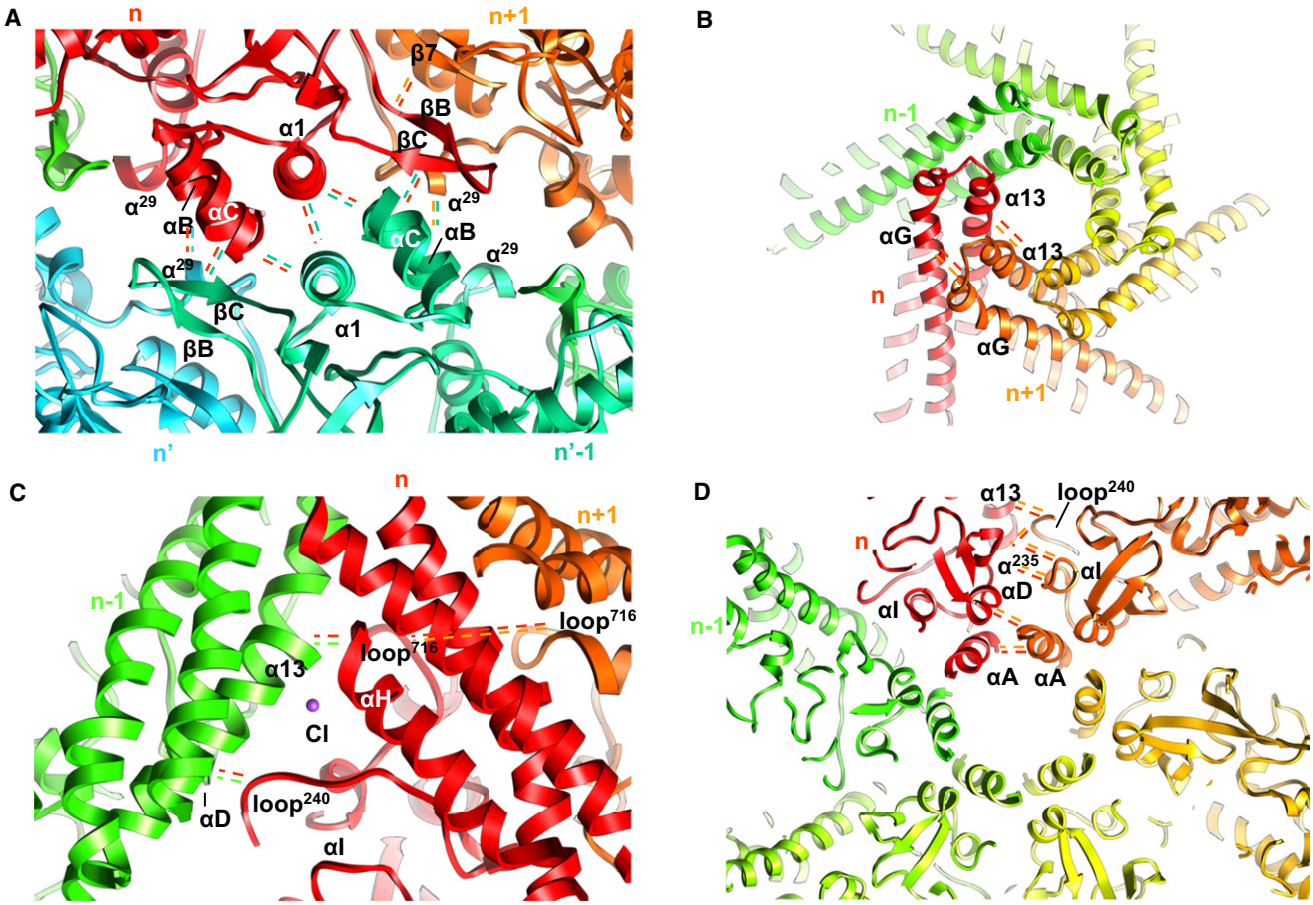

Figure 8. Interactions Responsible for the Novel Inter- and Intra-Ring Interfaces in *B. fragilis* GSIII

The interacting subunits are labeled relative to the nth subunit but their coloring is arbitrary. Interacting SSEs are labeled as in Figure S2, but new elements are introduced: a29, a235, loop240, and loop716 (superscript numbering representing the residue number at the midpoint of the SSE or loop). Interactions between SSEs are marked with dashed lines, which are colored according to the subunits involved.

(A) View down the 2-fold axis at the interface between subunits from opposite rings of the complex.

(B) View down the 6-fold axis looking toward the center of the complex.

(C) Closeup view of the metal ion binding site formed between by the C-terminal helical extensions from adjacent subunits within one ring.

(D) View down the 6-fold axis from the inside of the complex.

(Gill et al., 2002); 2bvc (Krajewski et al., 2005). GSII structures included: 2d3a, 2d3b, 2d3c (Unno et al., 2006); 2ojw, 2qc8, 2uu7 (Krajewski et al., 2008).

For the superposition of the entire oligomeric assemblies of GSIII and GSI, one GSI dodecamer was first aligned to the top ring of GSIII, considering only the "A" chain from each molecule, using the MATCHALIGN feature in CHIMERA (Pettersen et al., 2004; Meng et al., 2006). This procedure was then repeated for the alternate ring of the GSIII complex, thus bringing the second GSI dodecamer into alignment.

Quaternary Structure Analyses

Interacting interfaces were identified and selected in CHIMERA (Pettersen et al., 2004) and contact surface areas were determined from the output of PDBSUM

Table 2. Surface Area Changes upon Oligomerization in the GS Family

	Monomer	Ring			Double-ring					
	SA (10^3 Å^2)	SA (10^3 Å^2)	% buried	Intra-ring interface SA/subunit (10^3 Å^2)	SA (10^3 Å^2)	% buried	Δ% buried	Inter-ring interface SA/ subunit (10^3 Å^2)	% accessible SA for 3Å radius probe vs. 1.4 Å	Total interface SA/subunit (10^3 Å^2)
GSI[a]	21.3	109.1	14.4	1.5	184.9	27.6	13.2	2.8	71	4.3
GSII[b]	15.8	59.4	25.0	2.0	115.3	27.0	2.0	0.4	70	2.4
GSIII[c]	28.2	141.5	16.2	2.3	272.7	19.2	3.0	0.9	59	3.2

[a] Calculated from *S. typhimurium* GSI (Yamashita et al., 1989).

[b] Calculated from *Z. mays* GSII (Unno et al., 2006).

[c] Calculated from *B. fragilis* GSIII.

(Laskowski, 2001). Interaction distance plots were calculated by the CSU program running on the "Tools for Structure Prediction and Analysis Based on Complementarity with Environment" (SPACE) Web server (Sobolev et al., 2005).

ACCESSION NUMBERS

Coordinates and structure factor files have been deposited in the RCSB Protein Data Bank with accession code 3O6X.

SUPPLEMENTAL INFORMATION

Supplemental Information includes three figures and one table and can be found with this article online at doi:10.1016/j.str.2011.02.001.

ACKNOWLEDGMENTS

This work was supported by the National Research Foundation (NRF) of South Africa. Synchrotron access was supplied by the European Molecular Biology Laboratory. J.v.R acknowledges PhD scholarships from the NRF, University of Cape Town, and Cape Biotech Trust.

Received: October 21, 2010
Revised: January 31, 2011
Accepted: February 7, 2011
Published: April 12, 2011

REFERENCES

Adams, P.D., Afonine, P.V., Bunkóczi, G., Chen, V.B., Davis, I.W., Echols, N., Headd, J.J., Hung, L.W., Kapral, G.J., Grosse-Kunstleve, R.W., et al. (2010). PHENIX: a comprehensive Python-based system for macromolecular structure solution. Acta Crystallogr. D Biol. Crystallogr. *66*, 213–221.

Amaya, K.R., Kocherginskaya, S.A., Mackie, R.I., and Cann, I.K.O. (2005). Biochemical and mutational analysis of glutamine synthetase type III from the rumen anaerobe *Ruminococcus albus* 8. J. Bacteriol. *187*, 7481–7491.

Brunger, A.T. (2007). Version 1.2 of the Crystallography and NMR System. Nat. Protoc. *2*, 2728–2733.

CCP4 (Collaborative Computational Project, Number 4). (1994). The CCP4 Suite: Programs for Protein Crystallography. Acta Crystallogr. D Biol. Crystallogr. *50*, 760–763.

Cowtan, K. (2006). The Buccaneer software for automated model building. Acta Crystallogr. D Biol. Crystallogr. *62*, 1002–1011.

Denman, R.B., and Wedler, F.C. (1984). Association-dissociation of mammalian brain glutamine synthetase: effects of metal ions and other ligands. Arch. Biochem. Biophys. *232*, 427–440.

Eichinger, L., Pachebat, J.A., Glöckner, G., Rajandream, M.A., Sucgang, R., Berriman, M., Song, J., Olsen, R., Szafranski, K., Xu, Q., et al. (2005). The genome of the social amoeba *Dictyostelium discoideum*. Nature *435*, 43–57.

Eisenberg, D., Gill, H.S., Pfluegl, G.M., and Rotstein, S.H. (2000). Structure-function relationships of glutamine synthetases. Biochim. Biophys. Acta *1477*, 122–145.

Emsley, P., and Cowtan, K. (2004). Coot: model-building tools for molecular graphics. Acta Crystallogr. D Biol. Crystallogr. *60*, 2126–2132.

Evans, P. (2005). Scaling and assessment of data quality. Acta Crystallogr. D Biol. Crystallogr. *62*, 72–82.

Gibson, F.C., III, Onderdonk, A.B., Kasper, D.L., and Tzianabos, A.O. (1998). Cellular mechanism of intraabdominal abscess formation by *Bacteroides fragilis*. J. Immunol. *160*, 5000–5006.

Gill, H.S., and Eisenberg, D. (2001). The crystal structure of phosphinothricin in the active site of glutamine synthetase illuminates the mechanism of enzymatic inhibition. Biochemistry *40*, 1903–1912.

Gill, H.S., Pfluegl, G.M.U., and Eisenberg, D. (2002). Multicopy crystallographic refinement of a relaxed glutamine synthetase from *Mycobacterium tuberculosis* highlights flexible loops in the enzymatic mechanism and its regulation. Biochemistry *41*, 9863–9872.

Goodman, H.J.K., and Woods, D.R. (1993). Cloning and nucleotide sequence of the *Buyrivibrio fibrisolvens* gene encoding a type III glutamine synthetase. J. Gen. Microbiol. *139*, 1487–1493.

Goodsell, D.S., and Olson, A.J. (2000). Structural Symmetry and Protein Function. Annu. Rev. Biophys. Biomol. Struct. *29*, 105–153.

Grosse-Kunstleve, R.W., and Adams, P.D. (2003). Substructure search procedures for macromolecular structures. Acta Crystallogr. D Biol. Crystallogr. *59*, 1966–1973.

Harth, G., and Horwitz, M.A. (1999). An inhibitor of exported *Mycobacterium tuberculosis* glutamine synthetase selectively blocks the growth of pathogenic mycobacteria in axenic culture and in human monocytes: extracellular proteins as potential novel drug targets. J. Exp. Med. *189*, 1425–1436.

He, Y.X., Gui, L., Liu, Y.Z., Du, Y., Zhou, Y., Li, P., and Zhou, C.Z. (2009). Crystal structure of *Saccharomyces cerevisiae* glutamine synthetase Gln1 suggests a nanotube-like supramolecular assembly. Proteins *76*, 249–254.

Hill, R.T., Parker, J.R., Goodman, H.J., Jones, D.T., and Woods, D.R. (1989). Molecular analysis of a novel glutamine synthetase of the anaerobe *Bacteroides fragilis*. J. Gen. Microbiol. *135*, 3271–3279.

Kinoshita, S., Isu, S., Kaneko, G., Yamada, H., Hara, T., Itoh, Y., and Watabe, S. (2009). The occurrence of eukaryotic type III glutamine synthetase in the marine diatom *Chaetoceros compressum*. Marine Genomics *2*, 103–111.

Kleywegt, G.J., Zou, J.Y., Kjeldgaard, M., and Jones, T.A. (2006). Around O. In International Tables for Crystallography, Vol. F: Crystallography of Biological Macromolecules, M.G. Rossmann and E. Arnold, eds. (Dordrecht, Netherlands: Kluwer Academic Publishers), pp. 353–356, 366–367.

Krajewski, W.W., Jones, T.A., and Mowbray, S.L. (2005). Structure of *Mycobacterium tuberculosis* glutamine synthetase in complex with a transition-state mimic provides functional insights. Proc. Natl. Acad. Sci. USA *102*, 10499–10504.

Krajewski, W.W., Collins, R., Holmberg-Schiavone, L., Jones, T.A., Karlberg, T., and Mowbray, S.L. (2008). Crystal structures of mammalian glutamine synthetases illustrate substrate-induced conformational changes and provide opportunities for drug and herbicide design. J. Mol. Biol. *375*, 217–228.

Kretovich, W.L., Evstigneeva, Z.G., Pushkin, A.V., and Tsuprun, V.L. (1984). Evolution of the quaternary structure of glutamine synthetase. Quaderni de la Recerca Scientifica *113*, 109–115.

Kumada, Y., Benson, D.R., Hillemann, D., Hosted, T.J., Rochefort, D.A., Thompson, C.J., Wohlleben, W., and Tateno, Y. (1993). Evolution of the glutamine synthetase gene, one of the oldest existing and functioning genes. Proc. Natl. Acad. Sci. USA *90*, 3009–3013.

Kumada, Y., Takano, E., Nagaoka, K., and Thompson, C.J. (1990). Streptomyces hygroscopicus has two glutamine synthetase genes. J. Bacteriol. *172*, 5343–5351.

Laskowski, R.A. (2001). PDBsum: summaries and analyses of PDB structures. Nucleic Acids Res. *29*, 221–222.

Leslie, A.G. (2006). The integration of macromolecular diffraction data. Acta Crystallogr. D Biol. Crystallogr. *62*, 48–57.

Liaw, S.H., Pan, C., and Eisenberg, D. (1993). Feedback inhibition of fully unadenylylated glutamine synthetase from *Salmonella typhimurium* by glycine, alanine, and serine. Proc. Natl. Acad. Sci. USA *90*, 4996–5000.

Liaw, S.H., Jun, G., and Eisenberg, D. (1994). Interactions of nucleotides with fully unadenylated glutamine synthetase from *Salmonella typhimurium*. Biochemistry *33*, 11184–11188.

Llorca, O., Betti, M., González, J.M., Valencia, A., Márquez, A.J., and Valpuesta, J.M. (2006). The three-dimensional structure of an eukaryotic glutamine synthetase: Functional implications of its oligomeric structure. J. Struct. Biol. *156*, 469–479.

Lumry, R., and Rajender, S. (1970). Enthalpy-entropy compensation phenomena in water solutions of proteins and small molecules: a ubiquitous property of water. Biopolymers *9*, 1125–1227.

Mathis, R., Gamas, P., Meyer, Y., and Cullimore, J.V. (2000). The presence of GSI-like genes in higher plants: support for the paralogous evolution of GSI and GSII. J. Mol. Evol. *50*, 116–122.

McCoy, A.J., Grosse-Kunstleve, R.W., Adams, P.D., Winn, M.D., Storoni, L.C., and Read, R.J. (2007). Phaser crystallographic software. J. Appl. Crystallogr. *40*, 658–674.

McGuffin, L.J., Bryson, K., and Jones, D.T. (2000). The PSIPRED protein structure prediction server. Bioinformatics *16*, 404–405.

McRee, D.E., and Israel, M. (2008). XtalView, protein structure solution and protein graphics, a short history. J. Struct. Biol. *163*, 208–213.

Meng, E.C., Pettersen, E.F., Couch, G.S., Huang, C.C., and Ferrin, T.E. (2006). Tools for integrated sequence-structure analysis with UCSF Chimera. BMC Bioinformatics *7*, 339.

Monod, J. (1968). On Symmetry and Function in Biological Systems. Nobel Symp. Symmetry Funct. Biol. Syst. Macromol. Lev., 11th, Stockholm, 15-27. (New York: Wiley).

Nicholas, K.B., Nicholas, H.B., Jr., and Deerfield, D.W., II. (1997). GeneDoc: analysis and visualization of genetic variation. embnet.news *4*, 14.

Pesole, G., Bozzetti, M.P., Lanave, C., Preparata, G., and Saccone, C. (1991). Glutamine synthetase gene evolution: a good molecular clock. Proc. Natl. Acad. Sci. USA *88*, 522–526.

Pettersen, E.F., Goddard, T.D., Huang, C.C., Couch, G.S., Greenblatt, D.M., Meng, E.C., and Ferrin, T.E. (2004). UCSF Chimera—a visualization system for exploratory research and analysis. J. Comput. Chem. *25*, 1605–1612.

Reyes, J.C., and Florencio, F.J. (1994). A new type of glutamine synthetase in cyanobacteria: the protein encoded by the glnN gene supports nitrogen assimilation in *Synechocystis* sp. strain PCC 6803. J. Bacteriol. *176*, 1260–1267.

Reyes, J.C., Muro-Pastor, M.I., and Florencio, F.J. (1997). Transcription of glutamine synthetase genes (glnA and glnN) from the cyanobacterium *Synechocystis* sp. strain PCC 6803 is differently regulated in response to nitrogen availability. J. Bacteriol. *179*, 2678–2689.

Rhee, S.G., Chock, P., Wedler, F.C., and Sugiyama, Y. (1981). Subunit interaction in unadenylylated glutamine synthetase from *Eschericia coli*. J. Biol. Chem. *256*, 644–648.

Schüttelkopf, A.W., and van Aalten, D.M.F. (2004). PRODRG—a tool for high-throughput crystallography of protein-ligand complexes. Acta Crystallogr. D Biol. Crystallogr. *60*, 1355–1363.

Seabra, A.R., Carvalho, H., and Pereira, P.J.B. (2009). Crystallization and prelimary crystallographic characterization of glutamine synthetase from *Medicago truncatula*. Acta Crystallogr. Sect. F Struct. Biol. Cryst. Commun. *65*, 1309–1312.

Sharp, K., Fine, R., and Honig, B. (1987). Computer simulations of the diffusion of a substrate to an active site of an enzyme. Science *236*, 1460–1464.

Shatsky, M., Nussinov, R., and Wolfson, H.J. (2004). A method for simultaneous alignment of multiple protein structures. Proteins *56*, 143–156.

Shrake, A., Whitley, E.J., and Ginsburg, A. (1980). Conformational differences between unadenylylated and adenylylated glutamine synthetase from *Eschericia coli* on binding L-methionine sulfoximine. J. Biol. Chem. *255*, 581–589.

Sobolev, V., Eyal, E., Gerzon, S., Potapov, V., Babor, M., Prilusky, J., and Edelman, M. (2005). SPACE: a suite of tools for protein structure prediction and analysis based on complementarity and environment. Nucleic Acids Res. *33*, W39–W43.

Soper, D. (2004). Trichomoniasis: under control or undercontrolled? Am. J. Obstet. Gynecol. *190*, 281–290.

Southern, J.A., Parker, J.R., and Woods, D.R. (1986). Expression and purification of glutamine synthetase cloned from *Bacteroides fragilis*. J. Gen. Microbiol. *132*, 2827–2835.

Southern, J.A., Parker, J.R., and Woods, D.R. (1987). Novel structure, properties, and inactivation of glutamine synthetase cloned from *Bacteroides fragilis*. J. Gen. Microbiol. *133*, 2437–2446.

Terwilliger, T.C. (2000). Maximum likelihood density modification. Acta Crystallogr. D Biol. Crystallogr. *56*, 965–972.

Trapani, S., and Navaza, J. (2008). AMoRe: classical and modern. Acta Crystallogr. D Biol. Crystallogr. *64*, 11–16.

Unno, H., Uchida, T., Sugawara, H., Kurisu, G., Sugiyama, T., Yamaya, T., Sakakibara, H., Hase, T., and Kusunoki, M. (2006). Atomic structure of plant glutamine synthetase: a key enzyme for plant productivity. J. Biol. Chem. *281*, 29287–29296.

van Rooyen, J.M., Abratt, V.R., and Sewell, B.T. (2006). Three dimensional structure of the glutamine synthetase from *Bacteroides fragilis* by single particle reconstruction. J. Mol. Biol. *361*, 796–810.

van Rooyen, J.M., Abratt, V.R., Belrhali, H., and Sewell, B.T. (2010). Crystallization of recombinant Bacteroides fragilis glutamine synthetase (GlnN) isolated using a novel and rapid purification protocol. Protein Expr. Purif. *74*, 211–216.

van Rooyen, J.M., Belrhali, H., Abratt, V.R., and Sewell, B.T. (2011). Proteolysis of the type III glutamine synthetase from *Bacteroides fragilis* causes expedient crystal packing rearrangements. Acta Crystallogr. Sect. F Struct. Biol. Crystallogr. Commun. *67*, 358–363.

Waterhouse, A.M., Procter, J.B., Martin, D.M.A., Clamp, M., and Barton, G.J. (2009). Jalview Version 2 - a multiple sequence alignment editor and analysis workbench. Bioinformatics *25*, 1189–1191.

White, O., Eisen, J.A., Heidelberg, J.F., Hickey, E.K., Peterson, J.D., Dodson, R.J., Haft, D.H., Gwinn, M.L., Nelson, W.C., Richardson, D.L., et al. (1999). Genome sequence of the radioresistant bacterium *Deinococcus radiodurans* R1. Science *286*, 1571–1577.

Wriggers, W., Milligan, R.A., and McCammon, J.A. (1999). Situs: a package for docking crystal structures into low-resolution maps from electron microscopy. J. Struct. Biol. *125*, 185–195.

Wyatt, K., White, H.E., Wang, L., Bateman, O.A., Slingsby, C., Orlova, E.V., and Wistow, G. (2006). Lengsin is a survivor of an ancient family of class I glutamine synthetases re-engineered by evolution for a role in the vertebrate lens. Structure *14*, 1823–1834.

Xu, J., Bjursell, M.K., Himrod, J., Deng, S., Carmichael, L.K., Chiang, H.C., Hooper, L.V., and Gordon, J.I. (2003). A genomic view of the human—*Bacteroides thetaiotaomicron* symbiosis. Science *299*, 2074–2076.

Yamashita, M.M., Almassy, R.J., Janson, C.A., Cascio, D., and Eisenberg, D. (1989). Refined atomic model of glutamine synthetase at 3.5 Å resolution. J. Biol. Chem. *264*, 17681–17690.